

# SEGMENTATION OF PLANAR STRUCTURES IN BIOIMAGING

A. Martinez-Sanchez<sup>1</sup>, I. Garcia<sup>2</sup> and J. J. Fernandez<sup>3</sup>

<sup>1</sup>Grupo Supercomputacion y Algoritmos, Universidad de Almeria, Almeria, Spain

<sup>2</sup>Grupo Supercomputacion y Algoritmos, Universidad de Malaga, Malaga, Spain

<sup>3</sup>Centro Nacional de Biotecnologia (CSIC), Madrid, Spain

Keywords: Planar Structures, Segmentation, Feature Detection, Biomedical Imaging.

Abstract: This work presents an approach to detection of planar structures in three-dimensional (3D) datasets obtained by different bioimaging modalities. The strategy has already turned out to be effective to segment membranes from 3D volumes in the field of electron tomography, an emerging and powerful technique in structural and cellular biology. This approach can also be useful to detect planar structures in general in other bioimaging modalities. The goal of this position paper is to present this approach to the computer vision community and illustrate the performance on a number of representative bioimaging datasets.

## 1 INTRODUCTION

The advent of biological imaging has made it possible to observe, directly or indirectly, the molecular and cellular architecture and interactions that underlie essential functions within cells and tissues (Chandler and Roberson, 2009). The availability of imaging techniques (optical, confocal, electron microscopies, electron tomography, just to name a few) in biology laboratories is growing rapidly. So does the need for image processing methods that facilitate analysis and interpretation at different scales of resolution and complexity. In this regard segmentation, which intends to semantically decompose the datasets into their structural components, plays a central role.

Structures that can be considered as planes at local scale are often found in bioimaging datasets. Biological membranes are one of the best examples. Membranes encompass compartments within biological specimens, define the limits of the intracellular organelles and the cells themselves, etc. Detection of planar structures in general is important towards (semi-)automated segmentation of the whole datasets. Recently, we have presented an approach based on local differential information that succeeds in segmenting biological membranes (or any planar structure in general) in three-dimensional (3D) datasets obtained by electron tomography (ET) (Martinez-Sanchez et al., 2011). ET nowadays proves to be one of the leading techniques for visualizing the molecular organization of the cell environment (Frank, 2006; Lucic et al., 2005). In this field, manual segmentation still remains prevalent because no computational me-

thod has stood out as general applicable yet due to different reasons (they were case-specific, or limited performance under low signal-to-noise ratio, difficult parameter tuning, user-intervention required, etc) (Volkman, 2010). In manual segmentation, the user delineates the features of interest using visualization tools, which is tedious and subjective.

This position paper aims to present our approach to detect planar structures to the computer vision community and show its performance on datasets derived from different bioimaging modalities, including others than ET. Based on a Gaussian model for the thickness of the planes, the procedure relies on the characterization of structures at a local scale using differential information. Later, the integration at a global scale yields the definite detection.

## 2 DETECTION OF PLANES

### 2.1 Model for the Planar Structure

In experimental datasets and at a local level, the planar structure has certain thickness and the density along the direction normal to the plane progressively decreases as a function of the distance to the centre of the plane (Fig. 1) (Fernandez and Li, 2003; Fernandez and Li, 2005). This density variation can be modelled by a Gaussian function (Fig. 1):

$$I(r) = \frac{D_0}{\sqrt{2\pi}\sigma_0} e^{-\frac{r^2}{2\sigma_0^2}} \quad (1)$$

where  $r$  runs along the normal to the plane,  $D_0$  is a constant to set the maximum density value (at the centre of the plane) and  $\sigma_0$  is related to its thickness.

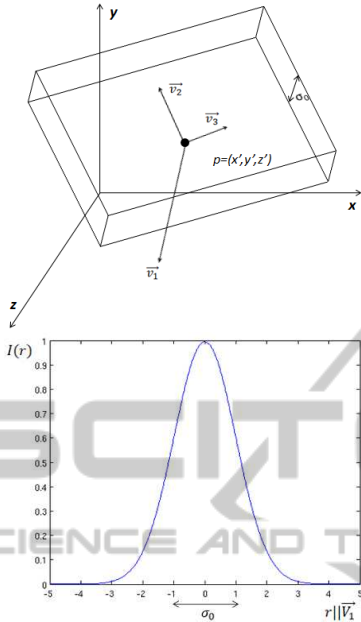


Figure 1: Plane model and the density profile across it.

The eigen-analysis of the density function at point  $p = (x, y, z)$  of the plane yields the eigenvectors  $\vec{v}_1$ ,  $\vec{v}_2$  and  $\vec{v}_3$  with eigenvalues  $|\lambda_1| \gg |\lambda_2| \approx |\lambda_3|$  (Fig. 1) (Fernandez and Li, 2003; Fernandez and Li, 2005). This reflects that there are two directions ( $\vec{v}_2$ ,  $\vec{v}_3$ ) with small density variation and the largest variation runs along the direction perpendicular to the plane ( $\vec{v}_1$ , parallel to  $r$ , i.e.  $\vec{v}_1 \parallel r$ ).

## 2.2 Scale-space

The scale-space theory was formulated in the 80s (Koenderink, 1984; Witkin, 1983) and allows isolation of the information according to the spatial scale. At a given scale  $\sigma$ , all the features with a size smaller than the scale are filtered out whereas the others are preserved. Therefore, the scale-space is useful to focus on the structures of a particular size, ignoring other smaller or spurious details. A scale-space for a volume  $f$  can be generated by convolving  $f$  with a set of kernels with size  $\sigma$  (Lindeberg, 1990). In this work we have used a recursive implementation of the Gaussian kernel with standard deviation  $\sigma$ ,  $G(x; \sigma)$  (Young and van Vliet, 1995).

To analyze the scale-space applied to the plane model, it can be assumed without loss of generality that  $r$  runs along the  $x$  direction (i.e.  $\vec{v}_1 \parallel r \parallel x$ ), hence

reducing the problem to one dimension (along  $x$ ). Given the Gaussian plane profile  $I$  (Eq. 1), ignoring constants, and taking into account that the convolution of two continuous Gaussian functions yields another Gaussian function whose variance is the sum of the variances (Florack et al., 1992), the plane model with thickness  $\sigma_0$  at a scale  $\sigma$  is:

$$L(x; \sigma) = G(x; \sigma) * I(x) = G(x; \sqrt{\sigma^2 + \sigma_0^2}) \quad (2)$$

## 2.3 Local Detector and Plane Strength

Now it is possible to define a detector for the plane model at a given scale  $\sigma$  (Eq. (2)). This detector is based on differential information, as it has to analyze local structure. In order to make it invariant to the plane direction, the detector is established along its normal (i.e. the direction of the maximum curvature) at the local scale. An eigen-analysis of the Hessian matrix is well suited to determine such direction (Frangi et al., 1998). At every voxel of the volume, the Hessian matrix is defined by:

$$H = \begin{bmatrix} L_{xx} & L_{xy} & L_{xz} \\ L_{xy} & L_{yy} & L_{yz} \\ L_{xz} & L_{yz} & L_{zz} \end{bmatrix} \quad (3)$$

where  $L_{ij} = \frac{\partial^2 I}{\partial i \partial j} \forall i, j \in (x, y, z)$ . The Hessian matrix provides information about the second order local intensity variation. The first eigenvector  $\vec{v}_1$  resulting from the eigen-analysis is the one whose eigenvalue  $\lambda_1$  exhibits the largest absolute value and points to the direction of the maximum curvature (second derivative).

The Hessian matrix of the plane model of the previous section (i.e. with maximum curvature along  $x$ ) at a scale  $\sigma$  has all directional derivatives null, except  $L_{xx}$ . As a result,  $\lambda_1 = L_{xx}$  and  $\vec{v}_1 = (1, 0, 0)$ . Along the direction normal to the plane,  $\lambda_1$  turns out to be negative where the plane has significant values and its absolute value progressively decreases from the centre towards the extremes of the plane, as shown in Fig. 2(top). Therefore, we propose the use of  $|\lambda_1|$  as a local plane detector (also known as local gauge). In practice, in experimental studies  $\lambda_2$  and  $\lambda_3$  are not null. Thus, a more realistic gauge would be:

$$R = \begin{cases} |\lambda_1| - \sqrt{\lambda_2 \lambda_3} & \lambda_1 < 0 \\ 0 & \lambda_1 \geq 0 \end{cases} \quad (4)$$

where  $\sqrt{\lambda_2 \lambda_3}$  is the geometrical mean between  $\lambda_2$  and  $\lambda_3$ .

Unfortunately,  $R$  is still sensitive to other local structures that may produce false positives along the maximum curvature direction. To make the gauge robust and more selective, it is necessary to define detectors for these cases. First, the noisy background

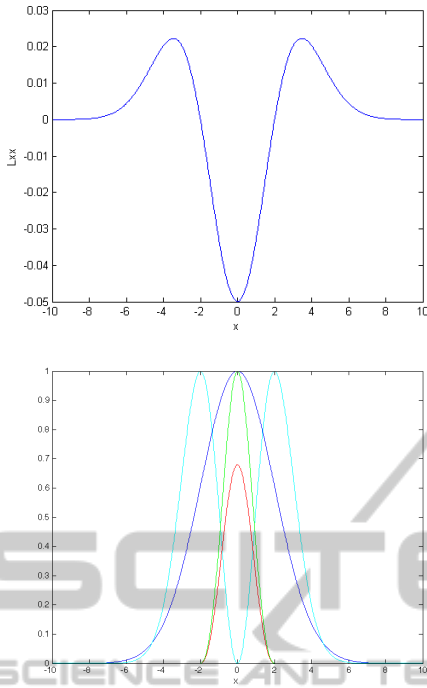


Figure 2: Second derivative  $L_{xx}$  of the plane model ( $\sigma_0 = 1$ ) at a scale  $\sigma = 1$  (top) and Gauges for the density profile of a plane with  $\sigma_0 = 1$  at a scale  $\sigma = 1$  (blue):  $R^2$  (red),  $S$  (cyan) and plane strength  $P$  (green). The profile across the plane,  $S$  and  $P$  are normalized in the range  $[0, 1]$ .  $R^2$  keeps the scale relative to  $S$ .

in the volume may generate false positives. However, the background usually has a density level different from that shown by the structures of interest. A strategy based on a density threshold  $t_l$  (Fernandez and Li, 2005) helps to get rid of these false positives.

Local structures resembling ‘density steps’ in the volume also make the gauge  $R$  produce a false peak. A suitable detector for a local step is the edge saliency (Lindeberg, 1998):

$$S = L_x^2 + L_y^2 + L_z^2 \quad (5)$$

where  $L_i = \frac{\partial I}{\partial i} \forall i \in (x, y, z)$ . A plane exhibits a high value of  $S$  at the extremes and a low value at the centre (Fig. 2(bottom)). Based on their response to a plane, the ratio between the squared second-order and first-order derivatives (i.e.  $R^2/S$ ) quantifies how well the local structure around a voxel fits the plane model and not a step. We thus define plane strength as:

$$P = \begin{cases} \frac{R^2}{S} & , (L > t_l) \text{ and } \left( \text{sign} \left( \frac{\partial R}{\partial r} \right) \neq \text{sign} \left( \frac{\partial S}{\partial r} \right) \right) \\ 0 & , \text{otherwise} \end{cases} \quad (6)$$

The first condition in Eq. (6) denotes the density thresholding described above. The second condition

represents the requirement that the slopes of  $R$  and  $S$  in the gradient direction must have opposite signs. This condition is important to restrict the response of that function for steps (see Fig. 2(bottom)). If the local structure approaches the plane model,  $P$  will have high values around the centre of the plane (high values of  $R^2$ , low values of  $S$ ).

## 2.4 Hysteresis Thresholding and Global Analysis

Due to the local nature of the plane model (see Subsection 2.1), any detector based on this model can also generate a high response for structures different from planar structures. For that reason, it is important to incorporate ‘global information’ to discern true planar structures from these others. The stages in this subsection are introduced for this purpose.

First, thresholding is applied to  $P$  in order to discard voxels unlikely belonging to planar structures. Hysteresis thresholding has been shown to outperform the standard thresholding algorithm (Sandberg, 2007). Here two thresholds are used, the large value  $t_u$  undersegments the volume whereas the other  $t_o$  oversegments it. Starting from the undersegmented volume (seed voxels), adjacent voxels are added to the segmented volume by progressively decreasing the threshold until the oversegmenting level  $t_o$  is reached.

Here we have increased the robustness of hysteresis thresholding by constraining the selection of seeds to the particular characteristics of planar structures in experimental biomedical datasets, namely the relatively high number of voxels connected. So, we have introduced two additional thresholds so that seed voxels belonging to components with less than  $t_a$  pixels slicewise, or  $t_h$  in 3D, are discarded. This allows isolation of seeds that are most representative of planar structures, thus improving the global performance.

Finally, a global analysis stage intends to identify the segmented components that are actually planar structures. A distinctive attribute is their relatively large dimensions. Therefore, the size (i.e. the number of voxels of the component) can serve as a major global descriptor. A threshold  $t_v$  (similar or equal to  $t_h$ ) is then introduced to set the minimal size for a component to be considered as a planar structure.

## 3 EXPERIMENTAL RESULTS

To illustrate the performance of the algorithm, it was tested with several volumes taken under different experimental conditions and with several bioimaging

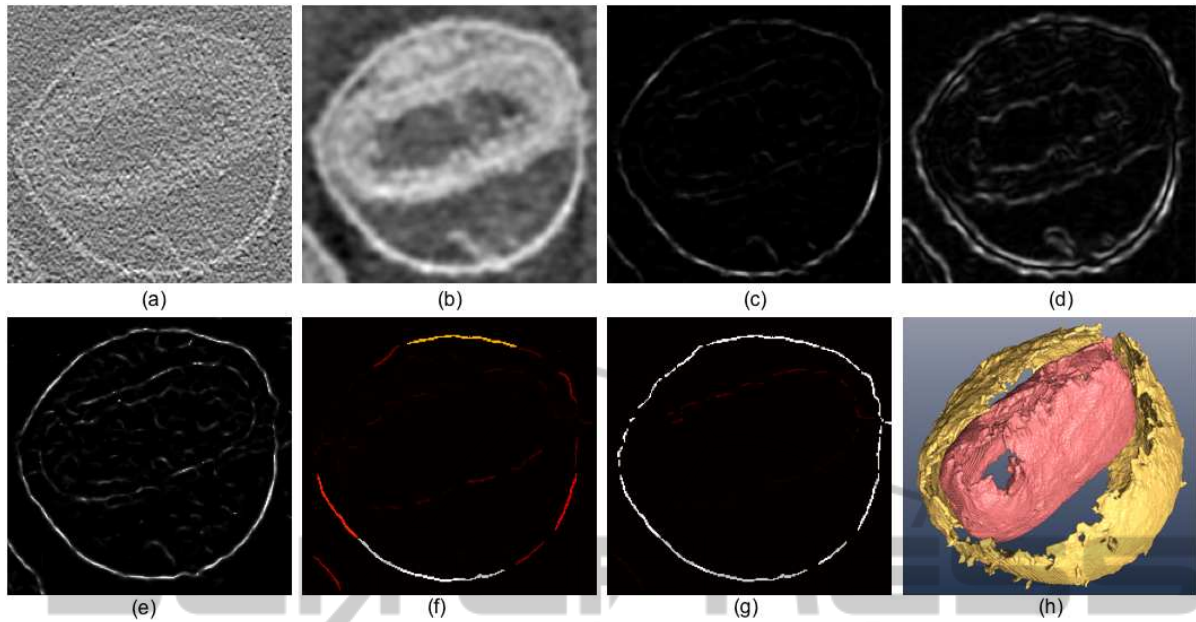


Figure 3: The procedure applied to a volume of Vaccinia virus obtained by electron tomography. (a) slice of the original volume. (b) at a scale  $\sigma = 3$ . (c-e)  $R$ ,  $S$  and  $P$ , respectively. (f, g) hysteresis thresholding. seed voxels to extract the outer membrane after the  $t_a$  and after  $t_h$  thresholding, respectively. brighter colour means larger number of connected voxels. (h) Membranes detected after the global analysis. The membrane of the internal core (in pink) was obtained after running the algorithm at a scale of  $\sigma = 6$ .

techniques. The volumes were rescaled to a common density range of  $[0, 1]$ . The optimal results were obtained using the same basic parameter configuration for hysteresis thresholding, in particular  $t_u \in [0.35, 1]$ ,  $t_o \in [0.05, 0.4]$  and  $t_a \in [15, 35]$ . The values of the parameters  $\sigma$ ,  $t_l$ ,  $t_h$  and  $t_v$ , however, depend on the specific dataset and were readily set by inspection of the volume.  $\sigma$  is the thickness of the sought planes, which were membranes in most of our tests.

First, to show the procedure at work, Fig. 3 shows the different stages applied to a volume of Vaccinia virus (Cyrklaff et al., 2005). This volume was obtained by electron tomography under low electron dose and cryogenic temperatures, which makes it particularly noisy and with low contrast. The algorithm succeeds in segmenting both the outer and the internal core membrane by properly tuning the parameter  $\sigma$ . A scale of  $\sigma = 3$  was applied to extract the outer membrane. For the core membrane, however, a much higher value was necessary ( $\sigma = 6$ ) because this membrane actually comprises two layers that make it rather thick, thereby needing a higher scale to extract it separately.

Fig. 3(c-e) (which were obtained at  $\sigma = 3$ , targeting at the outer membrane) clearly shows that, though the gauge  $R$  actually quantifies the level of local membrane-ness, it still depends on the density level. Thus, there are some parts of the membrane

where  $R$  exhibits weak values. On the contrary,  $P$  only contains differential information and, therefore, higher strength is shown throughout the membrane regardless of the density value. However, the side effect is that other structures resembling planes at local level also produce a high value of  $P$  (for instance, the dense material between the outer membrane and the core seen at the top of (e); or the fiber attached to the internal side of the outer membrane seen at the bottom of (e)). The hysteresis thresholding procedure and the global analysis then manage to extract the true membranes. This behaviour is an inherent feature of the algorithm.

To further illustrate the performance of the algorithm, it was applied to several volumes obtained by electron tomography and using experimental conditions that provides better contrast than in the previous case. The volumes contained different specimens, namely vesicles, mitochondrion and chloroplast, respectively. Fig. 4 shows a gallery of the structures, mostly membranes, detected by the algorithm. The algorithm was run at a scale  $\sigma$  of 2, 1.5 and 0.1, respectively. As shown, all the planar structures present in the volumes were clearly identified and come out of the background. The datasets were taken from the CCDB (Cell-Centered DataBase, <http://ccdb.ucsd.edu>) (Martone et al., 2008).

Finally, in order to demonstrate the applicabil-

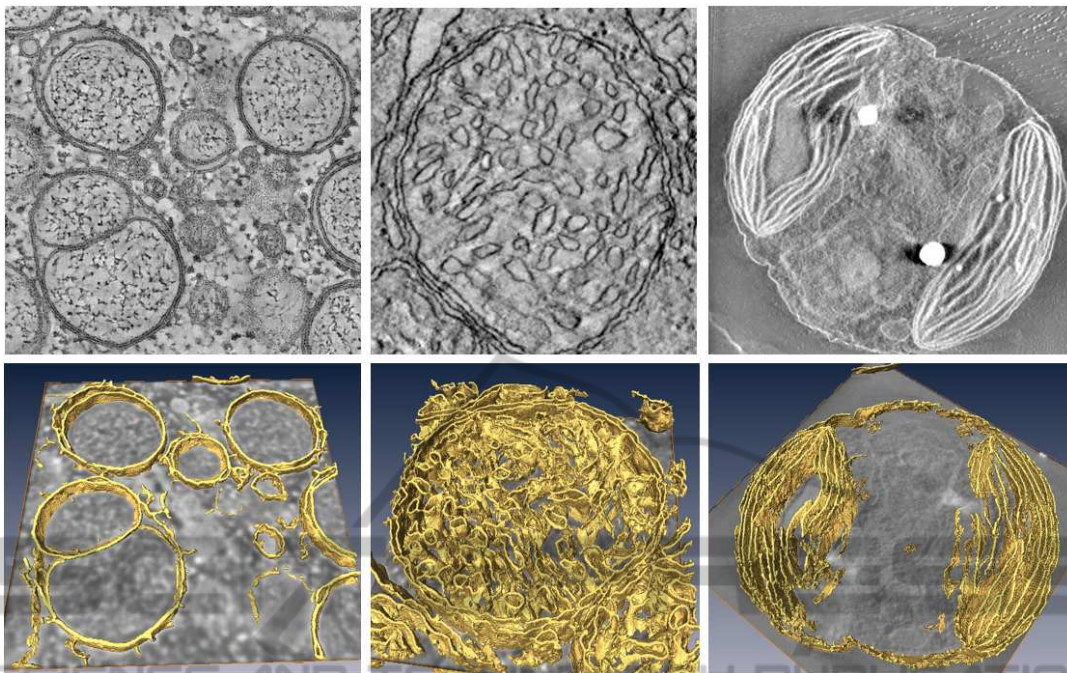


Figure 4: Planar structures detected by the algorithm for three different volumes containing vesicles, mitochondrion and chloroplast, respectively, that were obtained by electron tomography. Top: a slice of the original volume is shown. Bottom: 3D visualization.

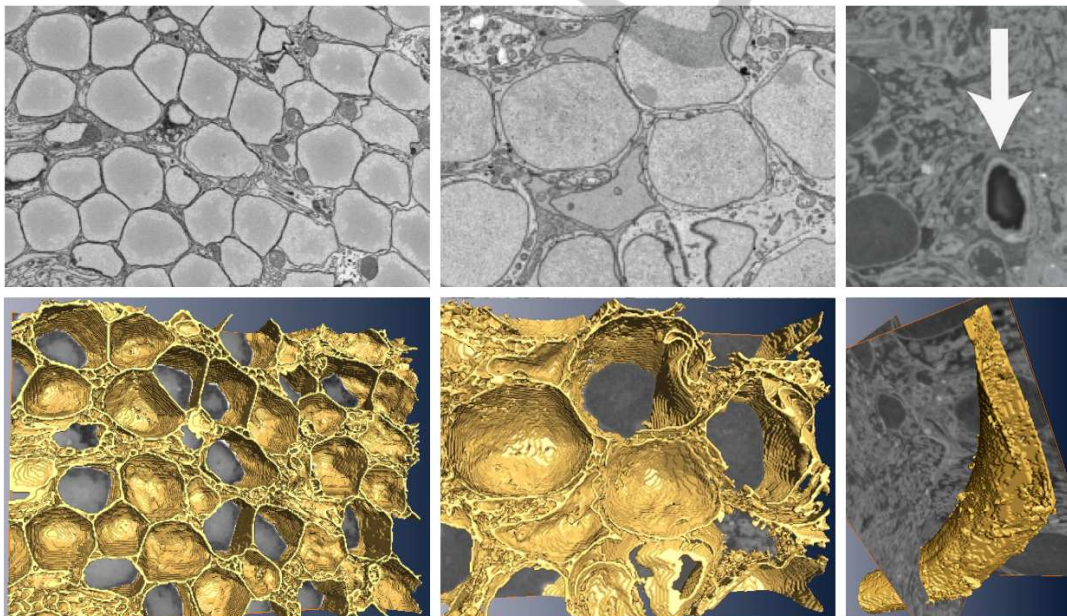


Figure 5: Planar structures detected by the algorithm for three representative areas of a thick retina tissue. Top: a slice of the original volume is shown. Bottom: 3D visualization of the planar structures.

ity of the algorithm to other bioimaging disciplines, we applied it to a volume derived from a study consisting in the ultrastructural characterization of the mouse optic nerve head and retina (Kim et al., 2010;

Nguyen et al., 2011), which was taken from the CCDB database (Martone et al., 2008). In this study, the thick tissue section was subjected to 3D reconstruction by a technique known as 'Serial Block Face

SEM' (SBFSEM). Here the tissue is progressively sliced into thin sections and the face of the remaining block is imaged by means of a Scanning Electron Microscope (SEM). At the end of the process, the images that were taken are stacked into a single volume, hence the 3D reconstruction. The tissue that was studied here contained different nerve cell layers. Figure 5 shows a gallery of representative areas of the different layers, where the segmentation of the planar structures performed by our algorithm is apparent. For these cases, the scale used in the application of the algorithm was 0.5.

## 4 CONCLUSIONS

We have presented a procedure to detect planar structures in volumes obtained by different bioimaging techniques. It relies on a simple local model for a plane and on the local differential structure to determine points whose neighbourhood resembles plane-like features. Later stages of the algorithm then intend to definitely determine which of those points do actually constitute the planar structures. The performance of algorithm has been shown on a set of representative volumes. In general, the algorithm has turned out to be effective to detect planar structures, often found in biological datasets. Therefore, it has potential to be a useful tool for (semi-)automated interpretation of 3D volumes obtained by different bioimaging technologies.

## ACKNOWLEDGEMENTS

Work supported by grants MCI-TIN2008-01117 and JA-P10-TIC6002. A.M.S. is a fellow of the Spanish FPI programme.

## REFERENCES

- Chandler, D. and Roberson, R. W. (2009). *Bioimaging: current techniques in light and electron microscopy*. Jones and Barlett Pub.
- Cyrklaff, M., Risco, C., Fernandez, J. J., Jimenez, M. V., Esteban, M., Baumeister, W., and Carrascosa, J. L. (2005). Cryo-electron tomography of vaccinia virus. *Proc. Natl. Acad. Sci. USA*, 102:2772–2777.
- Fernandez, J. J. and Li, S. (2003). An improved algorithm for anisotropic diffusion for denoising tomograms. *J. Struct. Biol.*, 144:152–161.
- Fernandez, J. J. and Li, S. (2005). Anisotropic nonlinear filtering of cellular structures in cryoelectron tomography. *Comput. Sci. Eng.*, 7(5):54–61.
- Florack, L. J., Romeny, B. H., Koenderink, J. J., and Viergever, M. A. (1992). Scale and the differential structure of images. *Image and Vision Computing*, 10:376–388.
- Frangi, A., Niessen, W., Vincken, K., and Viergever, M. (1998). Multiscale vessel enhancement filtering. *Lecture Notes in Computer Science*, 1496:130–137.
- Frank, J., editor (2006). *Electron tomography*. Springer.
- Kim, K., Ju, W., Hegedus, B., Gutmann, D., and Ellisman, M. (2010). Ultrastructural characterization of the optic pathway in a mouse model of neurofibromatosis-1 optic glioma. *Neuroscience*, 170:178–188.
- Koenderink, J. J. (1984). The structure of images. *Biol. Cybern.*, 50:363–370.
- Lindeberg, T. (1990). Scale-space for discrete signals. *IEEE Trans. PAMI*, 12(3):234–254.
- Lindeberg, T. (1998). Edge detection and ridge detection with automatic scale selection. *Int. J. Computer Vision*, 30:117–154.
- Lucic, V., Forster, F., and Baumeister, W. (2005). Structural studies by electron tomography: from cells to molecules. *Ann. Rev. Biochem.*, 74:833–865.
- Martinez-Sanchez, A., Garcia, I., and Fernandez, J. (2011). A differential structure approach to membrane segmentation in electron tomography. *J. Struct. Biol.*, 175:372–383.
- Martone, M., Tran, J., Wong, W. W., Sargis, J., Fong, L., and S. P. Lamont, S. L., Gupta, A., and Ellisman, M. H. (2008). The cell centered database: An update on building community resources for managing and sharing 3D imaging data. *J. Struct. Biol.*, 161:220–231.
- Nguyen, J., Soto, I., Kim, K., Bushong, E., Oglesby, E., Valiente, F., Yang, Z., Davis, C., Bedont, J., Son, J., Wei, J., Ellisman, M., and Marsh, N. (2011). Myelination transition zone astrocytes are constitutively phagocytic and have synuclein dependent reactivity in glaucoma. *Proc. Natl. Acad. Sci. USA*, 108:1176–1181.
- Sandberg, K. (2007). Methods for image segmentation in cellular tomography. *Methods in Cell Biology*, 79:769–798.
- Volkman, N. (2010). Methods for segmentation and interpretation of electron tomographic reconstructions. *Methods Enzymol.*, 483:31–46.
- Witkin, A. P. (1983). Scale-space filtering. In *Proc. 8th Intl. Conf. Artif. Intell.*, pages 1019–1022.
- Young, I. T. and van Vliet, L. J. (1995). Recursive implementation of the gaussian filter. *Signal Processing*, 44:139–151.